REPORT DOCUMENTATION PAGE

Form Approved
OMB No. 0704-0188

1. REPORT DATE (DD-MM-YYYY)	2. REPORT TYPE	3. DATES COVERED (From - To)
25-06-2003	Technical Paper	

4. TITLE AND SUBTITLE

Near Exit Plane Velocity Field of a 200 W Hall Thruster

5a. CONTRACT NUMBER

5b. GRANT NUMBER

5c. PROGRAM ELEMENT NUMBER

6. AUTHOR(S)

William Hargus; Christopher Charles

5d. PROJECT NUMBER
1011

5e. TASK NUMBER
0011

5f. WORK UNIT NUMBER

7. PERFORMING ORGANIZATION NAME(S) AND ADDRESS(ES)

Air Force Research Laboratory (AFMC)
AFRL/PRSS
1 Ara Drive
Edwards AFB CA 93524-7013

8. PERFORMING ORGANIZATION REPORT NUMBER

AFRL-PR-ED-TP-2003-175

9. SPONSORING / MONITORING AGENCY NAME(S) AND ADDRESS(ES)

Air Force Research Laboratory (AFMC)
AFRL/PRS
5 Pollux Drive
Edwards AFB CA 93524-7048

10. SPONSOR/MONITOR'S ACRONYM(S)

11. SPONSOR/MONITOR'S NUMBER(S)
AFRL-PR-ED-TP-2003-175

12. DISTRIBUTION / AVAILABILITY STATEMENT

Approved for public release; distribution unlimited.

13. SUPPLEMENTARY NOTES

For presentation at the AIAA Joint Propulsion Conference in Huntsville, AL, taking place 20-23 July 2003.

14. ABSTRACT

15. SUBJECT TERMS

16. SECURITY CLASSIFICATION OF:			17. LIMITATION OF ABSTRACT	18. NUMBER OF PAGES	19a. NAME OF RESPONSIBLE PERSON
a. REPORT	b. ABSTRACT	c. THIS PAGE			Leilani Richardson
Unclassified	**Unclassified**	**Unclassified**	A	9	19b. TELEPHONE NUMBER (include area code) (661) 275-5015

AIAA-2003-5154

Near Exit Plane Velocity Field of a 200 W Hall Thruster

William A. Hargus, Jr*
Lt. Christopher S. Charles**
Air Force Research Laboratory
Spacecraft Propulsion Branch
Edwards AFB, CA 93524

Abstract

This work presents the near exit plane velocity field of the Busek Company BHT-200-X3 200 W Hall thruster at a single operating condition with a 250 V anode potential. The ionized propellent velocities were measured using laser induced fluorescence of the $5d[4]_{7/2} - 6p[3]_{5/2}$ excited state xenon ionic transition at 834.7 nm. Ion velocities were interrogated from the acceleration channel exit plane to a distance 107 mm from the exit plane (3.3 exit plane diameters). Both axial and radial velocity were measured. A nearly uniform axial velocity profile of approximately 13,800 – 500 m/s (130 – 10 eV) was measured at the thruster exit plane. The maximum axial velocity measured 107 mm from the exit plane was 16,800 m/s (192 eV). The divergent flow exiting the thruster acceleration channel mixes downstream due to the coaxial thruster geometry. This mixing is made evident by regions of multiple radial and axial velocity components. These regions also exhibit broadened fluorescence line shapes which are indicative of collisions between the various velocity populations. The regions where this mixing/collisional behavior occurs correspond to the bright visible plume jet. A limited study at off-nominal conditions near a region of high insulator erosion indicates that the impinging ion energy on the center pole insulator is predictability changed by flow rates and anode potentials; however, it also appears to vary significantly with magnetic field strength.

Introduction

In order to better characterize the use of Hall thrusters for on-orbit applications, there is a need for improved understanding of the near exit plane ion velocity field. Spacecraft interaction models have been developed which utilize near exit plane plasma information to estimate plume divergence and interactions with spacecraft surfaces [1]. A major limitation of these models is the accuracy of available near exit plane plume data. This is compounded by external ion acceleration.

The goal of this study is to characterize the near plume velocity field of a 200 W Hall thruster using excited state ionic xenon laser induced fluorescence (LIF). LIF is a preferred diagnostic for the investigation of plasma in the near plume regions since it is a non-intrusive measurement. Unlike electrostatic probes, LIF will not perturb the local plasma, or thruster operation.

Xenon Ion Spectroscopy

The nine stable isotopes of xenon, the propellant most commonly used in Hall thrusters, each have a slight difference in their electron transition energies due to their differences in mass. The odd mass isotopes are further spin split due to nuclear magnetic dipole and electric quadrapole moments. Nuclei which have an odd number of protons and/or an odd number of neutrons posses an intrinsic nuclear spin $Ih/2\pi$, where I is integral or half-integral depending on whether the atomic mass is even or odd, respectively. For nuclei with non-zero nuclear spin (angular momentum), there exists an interaction of the nucleus with the electron shell. This interaction leads to the splitting of levels with angular momentum J into a number of components, each corresponding to a specific value of the total angular momentum F. The details of how this hyperfine spin splitting affects the spectra of xenon, and in particular with regard to the transition studied in this work, are described in more detail elsewhere [2].

*Senior member AIAA
**Member AIAA

For the results reported here, we probed the 834.7 nm electronic transition of singly ionized xenon. The isotopic and nuclear-spin effects contributing to the hyperfine structure of the $5d[4]_{7/2} - 6p[3]_{5/2}$ xenon ion transition has a total of 19 isotopic and spin split components. The hyperfine splitting constants which characterize the variations in state energies are only known for a limited set of energy levels. Unfortunately, the 834.7 nm xenon ion transition only has data on the nuclear spin splitting constants of the $6p[3]_{5/2}$ upper state, and no information is available on the transition dependent isotope shifts [3-5]. This makes modeling of the line shape somewhat speculative.

For velocity measurements, it is often convenient to probe optically accessible transitions for which there is incomplete knowledge of the isotopic and nuclear spin splitting constants. Manzella and others have previously used the $5d[4]_{7/2} - 6p[3]_{5/2}$ xenon ion transition at 834.7 nm to make velocity measurements in a Hall thruster plume [2,6-7]. A convenient feature of this transition is the presence of a relatively strong line originating from the same upper state ($6s[2]_{3/2} - 6p[3]_{5/2}$ transition at 541.9 nm [8]) which allows for nonresonant fluorescence collection. A nonresonant fluorescence scheme is preferred where there is the possibility of laser scattering from surfaces.

The local velocity is determined by the spatially resolved measurement of the Doppler shift of the absorbing ions. If an absorber has a velocity component u along the axis of the laser beam, it will absorb the light at a frequency shifted from that of stationary absorbers. The magnitude of this frequency shift $\delta\nu_{12}$ depends on the speed u along the laser beam axis

$$\delta\nu_{12} = \nu_{12}\frac{u}{c} \qquad (1)$$

where c is the speed of light. The Doppler shift of a species fluorescence profile away from the line center ν_{12} of stationary absorbers is in proportion to u [9].

Apparatus

The measurements we present in this work were performed in Chamber 6 at the Air Force Research Laboratory (AFRL) Electric Propulsion Laboratory at Edwards AFB, CA. Chamber 6 is a nonmagnetic stainless steel chamber which has a 1.8 m diameter and 3.0 m length. It has a measured pumping speed of 32,000 l/s on xenon. Pumping is provided by four single stage cryo-panels (APD single stage cold heads at ~25 K) and one 50 cm two stage APD cryo-pump (<12 K). Chamber pressure during thruster operation is approximately $5\text{x}10^{-6}$ Torr, corrected for xenon.

The thruster used for this test is the Busek Company BHT-200-X3 200W Hall thruster which has been described elsewhere [10]. Table 1 shows the typical operating conditions for the BHT-200-X3 thruster. During thruster operation, the parameters shown in Table 1 are monitored and recorded at a 1 Hz data rate.

Table 1: Nominal Thruster Operating Conditions

Anode flow	840 μg/s (Xe)
Cathode flow	98 μg/s (Xe)
Anode potential	250 V
Anode current	0.820 A
Keeper current	0.0 A
Magnet current	1.0 A
Heater current	0.0 A

Figure 1 shows a side-view diagram of the Hall thruster mounted in AFRL Chamber 6. The thruster is mounted on a three axes orthogonal computer controlled translation system. Figure 1 also shows the two orthogonal LIF probe beams and windows through which the beams enter the chamber. Figure 2 shows a top view of the laser optical train, collection optics, and one leg of the external probe optics.

The laser used is a New Focus Vortex tunable diode laser. It is capable of tuning approximate –50 GHz about a center wavelength of 834.7 nm. The 10 mW beam is passed through a Faraday rotator to eliminate feedback to the laser. The laser beam then passes through several beam pick-offs until it reaches a 50-50 beam splitter (BS) where it is split into two beams of equal power. The first beam, the axial probe beam shown in Figs. 1 and 2, is focused by a lens and enters the vacuum chamber through a window. A second probe beam, shown in Fig. 1 only, is directed from the optical bench via a periscope apparatus so that it enters the chamber from above the thruster and probes the velocity perpendicular to the first probe beam. Each probe beam is chopped at a unique frequency by choppers Ch2 (2 kHz) and Ch3 (2.8 kHz) for phase sensitive detection of the fluorescence signals.

The two wedge beam pick-offs (BS /) shown in Fig. 2 provide portions of the beam for diagnostic purposes. The first beam pick-off directs a beam to a photo-

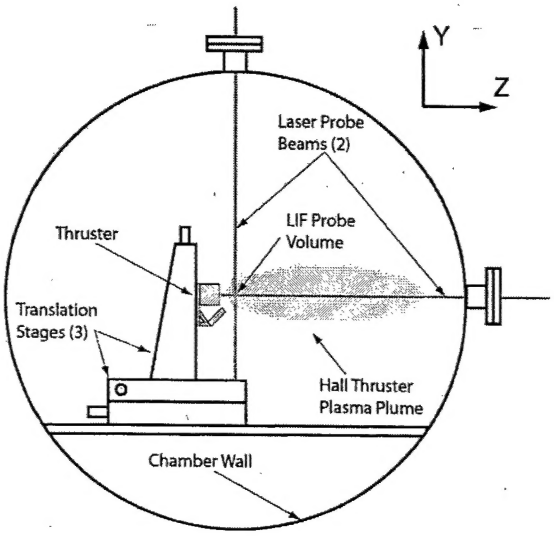

Fig. 1. Side view diagram of thruster within AFRL chamber 6. Also shown are the translation stages and the laser probe beams. Note that the fluorescence collection and external optics are not shown.

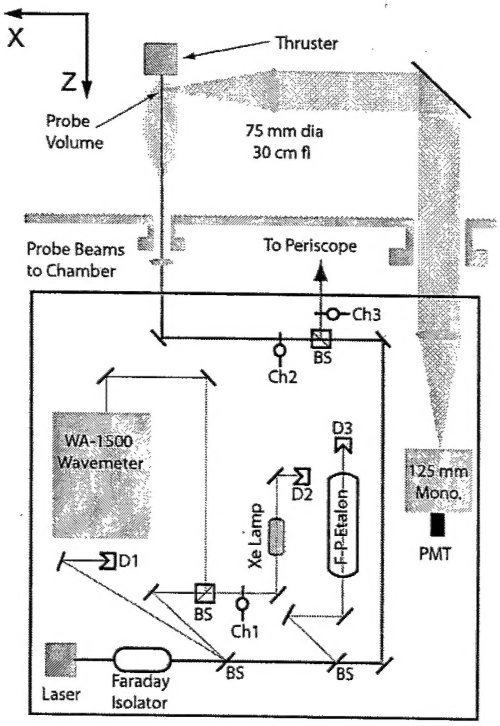

Fig. 2. Top view diagram of the laser optical train and collection optics. Note that the radial probe beam periscope and focusing optics are not shown.

diode detector (D1) used to provide constant power feedback to the laser. The second beam is divided into two equal components by a 50-50 beam splitter. The first component is directed to an Burleigh WA-1500 wavemeter used to monitor absolute wavelength. The second component is sent through chopper Ch1 (1.3 kHz) and through a low pressure xenon hollow cathode discharge lamp. The lamp provides a stationary absorption reference for the determination of the Doppler shift $\delta\nu_{12}$. Unfortunately, there is no detectable population of the ionic xenon $5d[4]_{7/2}$ state. However, there is a nearby (18.2 GHz distant) neutral xenon $6s'[1/2]_1^0$–$6p'[3/2]_2$ transition at 834.68 nm [11-12]. Absorption of this neutral xenon transition provides a stationary reference for measurement of the Doppler shifted ionic transition. The second pick-off sends a beam to a 300 MHz free spectral range Fabry-Perot etalon (F-P). This instrument provides high resolution frequency monitoring of the wavelength interval swept during a laser scan.

The fluorescence collection optics are also shown in Fig. 2. The fluorescence is collected by a 75 mm diameter, 300 mm focal length lens within the chamber. The collimated signal is directed through a window in chamber side wall to a similar lens that focuses the collected fluorescence onto the entrance slit of 125 mm focal length monochrometer with a Hamamatsu R928 photomultiplier tube (PMT) detector. Due to the 1:1 magnification of the collection optics, the spatial resolution of the measurements is determined by the geometry of the entrance slit 1 mm width and 1.7 mm height.

The laser is controlled by an analog ramp signal generated by a National Instruments E-series data acquisition board. During each laser scan, the data acquisition card records the absorption and two fluorescence signals using three lockin amplifiers. The signal from the Fabry Perot etalon photodiode detector (D3) signal is amplified and filtered using a current preamplifier. The output of which is also recorded. Typically, the scans span 55 GHz. Each scan yields four traces of several thousand points. The traces are then stored for post processing.

Figure 3 shows the near field geometry of the Busek BHT-200 Hall thruster. The locations of the central magnetic pole nose cone and edges of the acceleration channel are indicated as is the position of the cathode exit. The cartesian coordinate system and origin used in these measurements are also shown in Fig. 3. The coordinate system orientation is also referenced in Figs. 1 and 2. The origin is at the tip of the nose cone

due to the ease and repeatability with which this position could be located. All measurements presented in this work will be located using these coordinates. Furthermore, measurements presented in this work will be limited to the Y-Z plane.

Experimental Results

Figure 4 shows a sample LIF/absorption trace used to determine the velocity components of accelerated xenon ions (center of upper exit plane, Y= 12 mm, Z = -7 mm). The peak on the right hand side of the figure is the neutral $6s'[1/2]_1^0 - 6p'[3/2]_2$ transition absorption trace, rectified for clarity. At 18.2 GHz to the left is the position at which the ion $5d[4]_{7/2} - 6p[3]_{5/2}$ transition fluorescence would appear if the interrogated plasma were stationary. The left peak is the fluorescence signal extracted from the probe beam parallel to the Z axis (axial). The center peak is the signal from the probe beam parallel to the Y axis (radial since X = 0 for all measurements presented). In this case, the axial plasma velocity is 13,800 m/s and the radial velocity is -900 m/s. The length of the probe beam over which the velocities are averaged is 1 mm and 1.7 mm for the axial and radial measurements, respectively.

The uncertainty is estimated to be –500 m/s due to several factors. The first issue is the uncertainty in the relative neutral and ionic transition energies. The second issue concerns the resultant fluorescence line shapes. Figure 4 shows a reasonably sharp fluorescence line shape. However, close examination reveals a distinct low velocity component. The fluorescence line

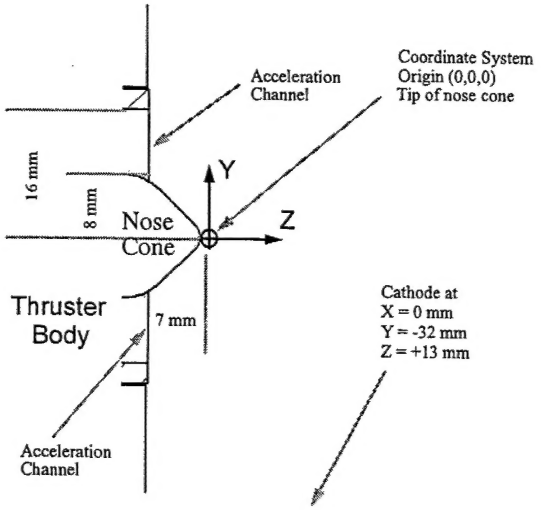

Fig. 3. Near field dimensions of the BHT-200 with origin of the coordinate system and positions of important locations noted.

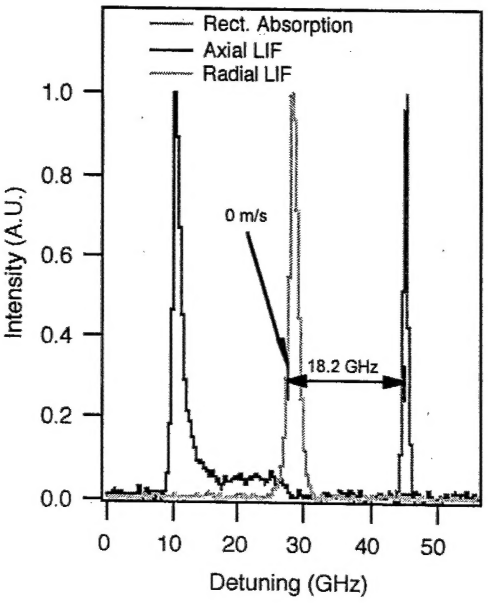

Fig. 4. Sample LIF / absorption trace. This particular trace was taken at the exit plane in the center of the acceleration channel. Note that all signals have normalized.

shapes measured in this study indicate the ion velocity is not a simple shifted Boltzman distribution. Rather, it is a convolution of a velocity distribution with a Doppler and possibly otherwise broadened line shape.

In this study, we have chosen to identify the peaks of the fluorescence line shapes as velocities. In the mixing portions of the flow, there is often more than one recognizable velocity population. In these cases, the distinct peaks are each assigned a velocity. In all these cases, the peaks are within the quoted uncertainty of –500 m/s, or better. In fact, the repeatability of the peak locations appear to be a fraction of the quoted uncertainty. However, the fluorescence line shapes are often significantly broadened, presumably due to wide velocity distributions. The quoted uncertainty should therefore be viewed as the uncertainty in the determination of the peak of the fluorescence line shape. In most cases, this will correspond to the velocity of the majority of the ion population. When multiple velocities are given for a single location, there may be ions with intermediate velocities.

Figures 5 and 6 show the velocity field measured in this study for the nominal operating conditions specified in Table 1. As shown in Fig. 5, the ions diverge as they emerge from the acceleration channel of the thruster. The ions are further accelerated axially, but

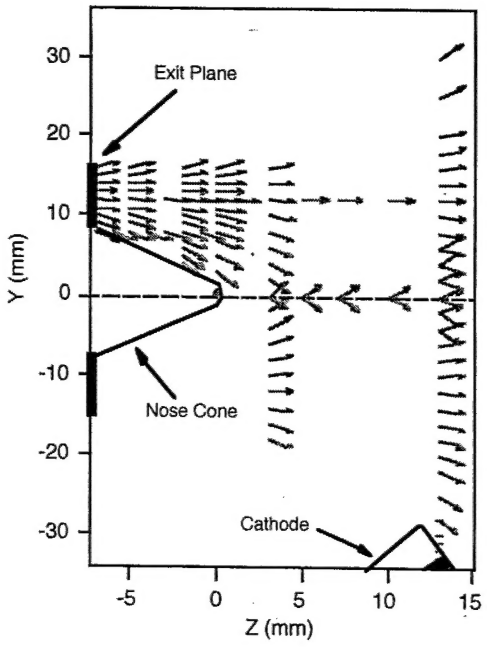

Fig. 5. Near exit plane velocity field of the BHT-200 for the operating conditions specified in Table 1.

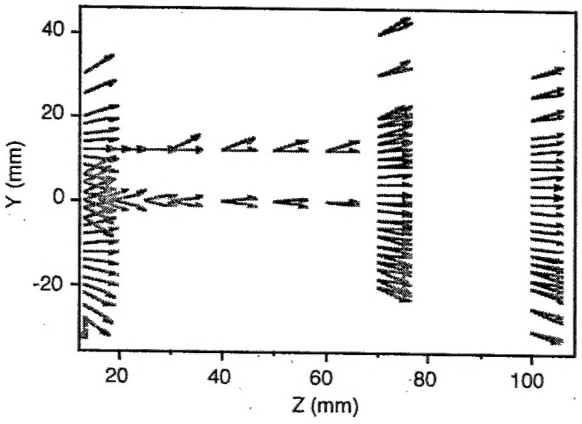

Fig. 6. Velocity field beyond the cathode plane of the BHT-200 for the conditions specified in Table 1.

continue to diverge, particularly near the thruster nose cone. Beyond the nose cone, the most striking feature of the flow field is the appearance of the mixing of distinct ion velocity populations which appear to originate from opposite sides of the nose cone. This mixing of divergent velocity populations begins near the nose cone tip (Z = 0 mm), but appears most noticeably near the cathode plane (Z = 13 mm). Further downstream, the divergent flows produce a central core with low radial velocities. This core is in turn surrounded by a sheath where there appear to be more than one velocity population. The sheath behavior occurs where there is a broad distribution within the radial velocity distribution. This is consistent with a region where large numbers of ion-ion momentum transfer collisions occur. Furthermore, these regions correspond with the plume jet typically exhibited by Hall thrusters.

Figure 7 shows the velocity profile at the exit plane. The axial velocity component is approximately uniform at 13,800 m/s (130 – 10 eV). The radial velocity varies continuously from 3,500 to -6000 m/s (~ 8 to 25 eV). The flow is approximately symmetrically divergent about the center of the acceleration channel (Y = 12 mm); however, the greatest radial velocity occurs nearest the boron nitride nose cone covering the central magnetic pole. This area has also exhibits significant erosion which manifests itself as a ring of material eroded from the nose cone base.

Figure 8 shows a cross-section of the velocity field at 3 mm beyond the tip of the nose cone (Z = 3 mm). Here, the axial velocity has increased to a maximum of 16,500 m/s (~185 eV), but is no longer cross-sectionally uniform. The dip about the thruster centerline (Y = 0) is caused by the flow of ions around the nose cone. The radial velocities peak at nearly –10,000 m/s (68 eV) and are, as would be expected, symmetric about the thruster. At this axial location, the majority of the energy has been electrostatically deposited into the propellant.

At the cathode plane (Z = 13 mm), the velocity profile looks similar to that seen in Fig. 8. In Fig. 9, the

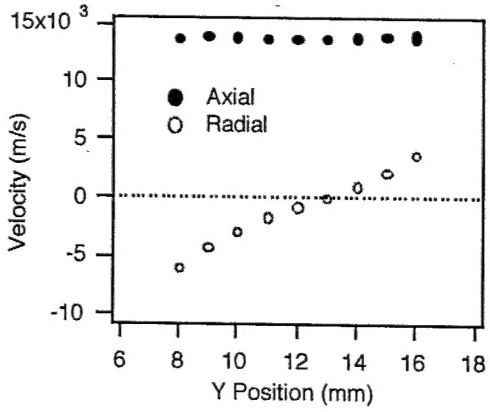

Fig. 7. Exit plane (Z = -7 mm) velocity field. Note the divergence, especially toward the center magnetic pole at Z =0.

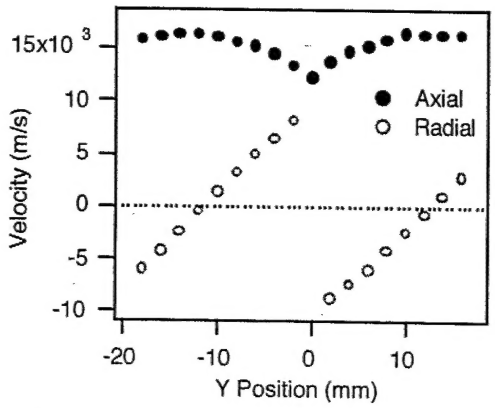

Fig. 8. Velocity field 3 mm beyond the nose cone, (Z = 3 mm). Note the symmetrical divergence and the turning of the flow around the thruster nose cone.

propellent has not been accelerated significantly past the previous maximum of nearly 16,500 m/s. However, two features are of interest. First, the influence of the cathode flow produces low velocities near the cathode exit. Second, the mixed flow regime is larger. In addition to the multiple radial velocity components, several locations have multiple axial velocity components. A more subtile change from the previous velocity profile is a slight flattening of the axial velocity profile. It should be noted that although the multiple radial velocity components are denoted here as single points, they often contain broader distributions than seen elsewhere in the plume.

The axial velocity profile continues to flatten as shown in Fig. 10, at Z = 100 mm. The velocity of the

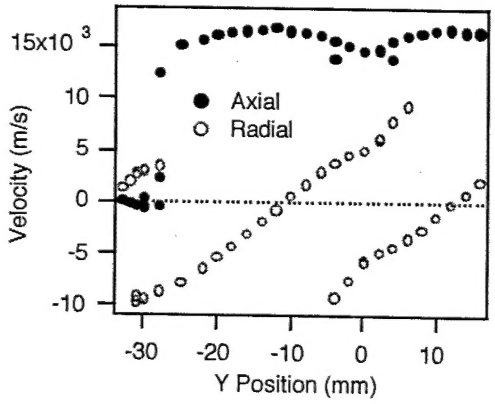

Fig. 9. Velocity field at cathode plane 13 mm beyond the nose cone, (Z = 13 mm). Note low velocity region near the cathode. Also note mixing of the flows from upper and lower acceleration channels as denoted by multiple velocity components.

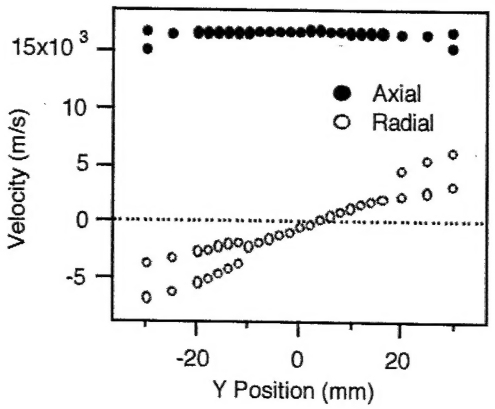

Fig. 10. Velocity field at Z = 100. Note flattened axial velocity distribution. Also note multiple velocity vectors in sheath flow.

axial velocity component has increased slightly increasing the peak axial directed kinetic energy of the xenon ions to 192 eV (16,800 m/s). The flow has evolved into a slightly divergent central flow surrounded by a sheath where mixing of more than one velocity group is also occurring. Since this position was the maximum axial distance examined, it is assumed that this characteristic behavior extends further. Ion current collection measurements of the far field plume (Z ~ 600 mm) show structure in the core portions of the flow. It may be possible to correlate the LIF derived velocities in this work to the ion fluxes measured in previous experiments [10].

Profiles of the external acceleration of the xenon ions are shown for two radial locations in Figs. 11 and 12. Figure 11 shows the ion axial and radial velocity components starting at the center of the upper acceleration channel (Y = 12 mm) from the exit plane to Z = 100 mm. Figure 12 shows the velocity components at the centerline of the thruster (Y = 0) beginning at the tip of the nose cone (Z = 0). These two figures show some interesting features of the BHT-200-X3 Hall thruster plume dynamics.

Figure 11 illustrates the extent of the acceleration occurring outside the thruster acceleration channel. The propellent exits the thruster at approximately 13,800 m/s and accelerates to a maximum axial velocity of 16,800 m/s. The propellent ions gain approximately 58 eV in this process. At this radial location (Y = 12 mm), the first evidence of mixing velocity groups appears at Z = 25 mm. At approximately Z = 50 mm, the multiple axial peaks can no longer be separated. The apparent drop in axial velocity at this location is an artifact of this issue and should not be construed as actual

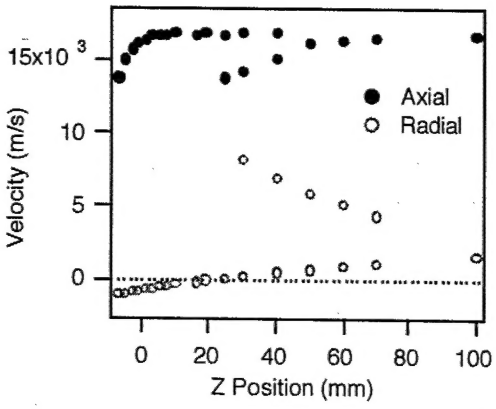

Fig. 11. Velocity profile at center of the acceleration channel (Y = 12 mm) from exit plane to Z = 100 mm.

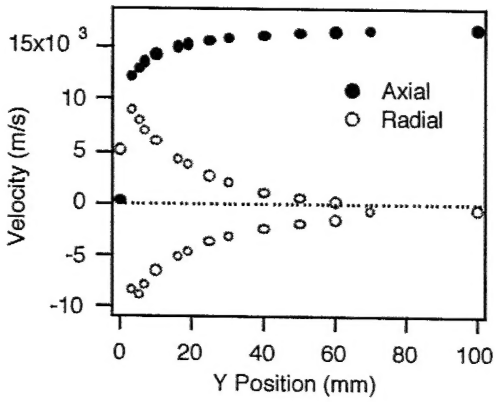

Fig. 12. Velocity profile at center of the thruster (Y = 0 mm) from tip of nose cone to Z = 100 mm.

deceleration of the xenon ions. Rather, it is an average velocity of the two velocity populations.

Figure 12 provides an alternative view of the external acceleration. Here we see the acceleration starting at the nose cone (Z = 0) and extending to the Z = 100 mm. The extent of the acceleration in Fig. 12 is less than in Fig. 11 since the start point is 7 mm further downstream. The initially lower velocities in Fig. 12 are due to the distance required for radial ion diffusion to populate the plume core. The diffusion manifests itself in Figs. 8-10, which exhibit an increasingly shallow gull-wing axial velocity component profiles. The apparently immense axial acceleration near the nose cone (Z = 0) is due to a population of slow moving ions located in the lee the nose cone. Although the mean velocity at this location is approximately zero, the fluorescence line shape is very broad at this location. The plasma at this location appears to have a broadly distributed velocity distribution. Physical evidence of high energy ions at this location possessing negative axial velocity is apparent from a pit which forms at the nose cone tip, presumably due to ion bombardment.

Figure 12 also shows the increasingly axial plume core flow. From the nose cone to approximately 70 mm, the central flow is dominated by a mixing of divergent radial flows. Beyond 70 mm, the flow along the plume centerline is nearly entirely axial with only small radial velocity components.

An extension to the measurements at the nominal operating conditions presented in Table 1 is shown in Fig. 13. Here, we show the radial energies directed toward the nose cone at Y = 8 mm from the exit plane to the tip of the nose cone. Six distinct operating conditions are shown; the nominal condition and 5 off-nominal conditions. These off-nominal conditions include decreased magnetic field strength, increased/decreased discharge voltage, and increased/decreased anode flow.

Erosion of the nose cone is a possible life limiting mechanism. Erosion is dependent on both the energy and flux of the impacting ions. Figure 13 provides an indication of the changes in relative erosion rate at the nose cone likely to occur by operation at conditions other than those shown in Table 1. As would be expected, the data is bracketed by operation at the high and low discharge potentials (300 V and 200 V versus a nominal 250 V). Most interesting is the significant increase of ion radial energy exhibited by operation at a reduced magnetic current strength (0.5 A versus a nomi-

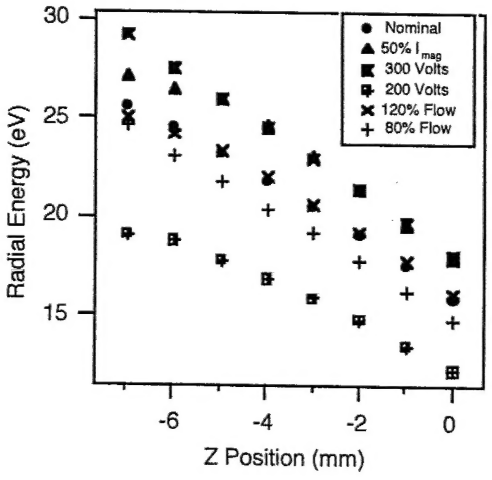

Fig. 13. Radial ion energies at Y = 8 mm for a range of Z locations for six operating conditions.

nal 1.0 A). In this case, the anode current did not rise significantly (840 mA versus a nominal 820 mA); however, the resultant decrease in thruster magnetic field increased the radial velocity component significantly. In fact, the flow angles for this case increased inward by approximately 2 degrees at the nose cone base and 1 degree near the tip. Finally, it should be noted that the erosion rate is not only a function to the directed ion energy, but is also proportional to flux. It may be assumed that the ion flux is approximately increased in proportion to the anode flow rate. This is important in the examination of the two cases in Fig. 13 which vary the anode propellent flow rate.

Conclusions

The velocity field for the near plume region of a 200 W Busek BHT-200-X3 Hall thruster has been mapped for a single operating condition. The measurements indicate that approximately 130 eV ions emerge from the thruster. These ions are accelerated to 185 eV between the exit plane and the cathode plane and eventually reach a maximum axial directed energy near 192 eV. This is consistent with the applied 250 V acceleration voltage. Previous measurements on other thrusters have shown a similar difference of approximately 50 V between the maximum ion energy and discharge voltage which has been attributed to the combined anode and cathode falls [2].

The flow field itself is shown to be a complex flow with mixing of distinct velocity populations. The mixing behavior becomes significant beyond the tip of the central magnetic pole nose cone. Further downstream at approximately 80 mm from the exit plane, the divergent flows produce a central core with small radial velocity components. This core is in turn surrounded by a sheath where there appears to be more than one velocity population. The sheath appears to be representative of collisions within the plume and is believed to be responsible for the core jet exhibited by Hall thruster plumes. The central plume core appears to be due to the diffusion of the plume ions into the central core region, most likely due to a potential difference between the acceleration channel center and the thruster centerline. This is consistent with lines of equipotential following expected lines of magnetic flux. Such a plume plasma potential structure would inhibit ions within the central core from exiting. It would also direct the flow in a nearly parallel beam consistent with the axial core flow. This supposition appears consistent with visual inspection of the plume during routine operation shown in Fig. 14. Here, we see the extent of the central jet feature which visibly extends to the same location as the multiple radial velocities shown in Fig. 12. The bright jet feature appears in the same regions where multiple velocity populations appear to be interacting, presumably through momentum transfer collisions, as shown in Figs 5 and 6. The plume jet appears to be a product of collisional interactions between multiple ion streams. These ions appear to have reasonably well defined axial velocity components, but broader distributions in their radial velocity components.

In this work, we examine the ion flow directed toward the central magnetic pole boron nitride nose cone and show that changing the operating conditions varies the ion flow impinging on it. The velocity measurements may also provide an indication of the relative erosion rate for various portions of the Hall thruster. The most intriguing finding is that lowering the magnetic field while maintaining an essentially nominal anode current increases the divergence of the propellent flow and will likely result in an increase of the erosion rate of the boron nitride nose cone.

Future Work

This effort has only partially examined the near exit plane velocity field of one operating condition and a small portion of several others. In order to fully characterize this thruster, several other operating conditions need careful examination. The capability to examine local velocities will be an asset in assessing the performance and lifetime of various Hall thrusters. However,

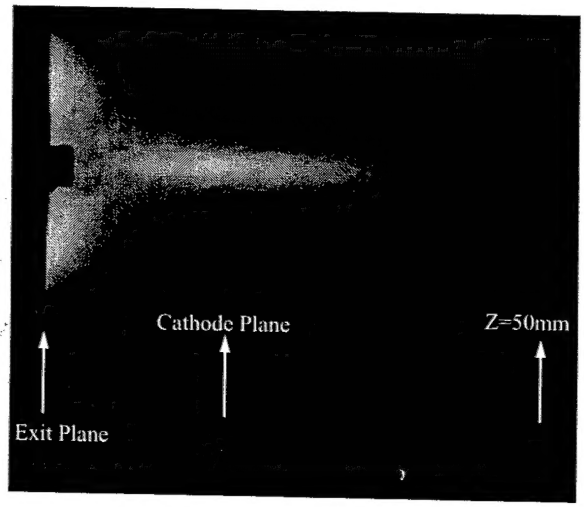

Fig. 14. Photograph of the BHT-200 Hall thruster plume operating at nominal conditions. Note similarities to vector fields presented in Figs. 5 and 6 as well as the velocity profile in Fig. 12.

several refinements would increased the value of these measurements.

The concept of a single velocity, even several distinct velocities, is inadequate, particularly in regions where significant mixing velocity populations is occurring. One approach that would provide a more accurate analysis of the true dynamics would be to extract a velocity distribution function from each of the fluorescence signals. This would provide an clearer interpretation of the velocity measurements. Due to the lack of the hyperfine spin splitting components of this transition, only an approximate line shape function could be constructed. However, this will be adequate to provide a reasonable indication of the velocity distribution function at each location. Several saturation studies were performed during testing which reveal that the fluorescence signal is not saturated. We plan to continue the analysis of the data to extract velocity distribution functions for later publication.

Another question for which the answer is imperfectly understood is the effect of increasing background pressure on operation of a Hall thruster. We plan to compare our data to data from a BHT-200-X3 operating at increased background pressure. Comparing spatially resolved velocity distributions for the two cases may provide information on the effects and extent of background xenon ingestion.

References

1. J.M. Fife, M.R. Gibbons, W.A. Hargus, D.B. VanGilder, D.E. Kirtley, and L.K. Johnson, 3-D Computation of Surface Sputtering and Redeposition Due to Hall Thruster Plumes, IEPC-2003-0136, *28th International Electric Propulsion Conference,* 17-21 Mar. 2003, Toulouse, France.
2. W. A. Hargus, Jr and M. A. Cappelli, Laser-Induced Fluorescence Measurements of Velocity within a Hall Discharge, *Applied Physics B,* Vol. 72, pp 961-969, 2001.
3. H. Geisen, T. Krumpelmann, D. Neuschafer, and Ch. Ottinger, Hyperfine Splitting Measurements on the 6265 and 6507 Lines of Seven Xe Isotopes by LIF on a Beam of Metastable Xe($^3P_{0,3}$) Atoms, *Physics Letters A,* Vol. 130, No. 4.5, 11 July, 1988.
4. W. Fischer, H. Huhnermann, G. Kromer, and H.J. Schafer, Isotope Shifts in the Atomic Spectrum of Xenon and Nuclear Deformation Effects, *Z. Physik,* Vol. 270, No. 113, 1974.
5. L. Bronstrom, A. Kastberg, J. Lidberg, S. Mannervik, Hyperfine-structure Measurements in Xe II, *Physical Review A,* Vol. 35, No. 1, Jan. 1996.
6. D.H. Manzella, Stationary Plasma Thruster Ion Velocity Distribution, AIAA-94-3141, 3 *0th Joint Propulsion Conference,* 27-29 June 1994, Indianapolis, IN.
7. J.E. Pollard and E.J. Beiting, Ion Energy, Ion Velocity, And Thrust Vector Measurements For The SPT-140 Hall Thruster, *3rd International Conference on Spacecraft Propulsion,* 10-13 Oct. 2000, Cannes, France.
8. J. E. Hansen and W. Persson, Revised Analysis of Singly Ionized Xenon, Xe II, *Physica Scripta,* Vol. 36, pp 602-643, 1987.
9. W. Demtroder, *Laser Spectroscopy: Basic Concepts and Instrumentation,* Springer-Verlag, Berlin, 1996
10. W.A. Hargus, Jr. and G. Reed, The Air Force Clustered Hall Thruster Program, AIAA-2002-3678, *38th Joint Propulsion Conference,* 7-10 July 2002, Indianapolis, Indiana.
11. M.H. Miller and R.A. Roig, Transition Probabilities of Xe I and Xe II, *Physical Review A,* Vol. 8, pp 480-486, July 1973.
12. C.E. Moore, *Atomic Energy Levels: Volume II,* Washington: National Bureau of Standards, pp 113-123, 1958.